CrossMark

A First Look into the Nature of JWST/MIRI 7.7 μm Sources from SMACS 0723

Edoardo Iani[1] , Karina I. Caputi[1,2] , Pierluigi Rinaldi[1] , and Vasily I. Kokorev[1,2,3]
[1] Kapteyn Astronomical Institute, University of Groningen, P.O. Box 800, 9700AV Groningen, The Netherlands; iani@astro.rug.nl, E.Iani@rug.nl
[2] Cosmic Dawn Center (DAWN), Jagtvej 128, DK-2200 Copenhagen N, Denmark
[3] Niels Bohr Institute, University of Copenhagen, Blegdamsvej 17, DK-2100 Copenhagen Ø, Denmark
Received 2022 August 12; revised 2022 October 15; accepted 2022 October 31; published 2022 November 22

Abstract

Until now, our knowledge of the extragalactic universe at mid-infrared (mid-IR) wavelengths ($>5\,\mu$m) was limited to rare active galactic nuclei and the brightest normal galaxies up to $z \sim 3$. The advent of JWST with its Mid-Infrared Instrument (MIRI) will revolutionize the ability of the mid-IR regime as a key wavelength domain to probe the high-z universe. In this work we present a first study of JWST MIRI 7.7 μm sources selected with $>3\sigma$ significance from the lensing cluster field SMACS J0723.3-7327. We model their spectral energy distribution (SED) fitting with 13 JWST and Hubble Space Telescope broad bands, in order to obtain photometric redshifts and derived physical parameters for all these sources. We find that this 7.7 μm galaxy sample is mainly composed of normal galaxies up to $z = 4$ and has a tail of about 2% of sources at higher redshifts to $z \approx 9$–10. The vast majority of our galaxies have [3.6]–[7.7] < 0 colors and very few of them need high dust extinction values ($A_V = 3$–6 mag) for their SED fitting. The resulting lensing-corrected stellar masses span the range 10^7–$10^{11}\,M_\odot$. Overall, our results clearly show that the first MIRI 7.7 μm observations of deep fields are already useful to probe the high-redshift universe and suggest that the deeper 7.7 μm observations to be available very soon will open up, for the first time, the epoch of reionization at mid-IR wavelengths.

Supporting material: machine-readable table

1. Introduction

Our knowledge of the extragalactic background sky has significantly improved over past decades with observations from space and ground-based observatories operating at different wavelengths. In the mid-infrared (mid-IR) regime (3–30 μm), in particular, a major leap forward has been achieved with the Spitzer Space Telescope (Spitzer, Werner et al. 2004), which has shown the important contribution of mid-IR wavelengths to the general extragalactic background light (Dole et al. 2006).

Moreover, Spitzer observations allowed us for the first time to reveal the high-redshift universe at mid-IR wavelengths (see, e.g., Bradač 2020, and references therein). Using the Infrared Array Camera (IRAC; Fazio et al. 2004) 3.6 and 4.5 μm, numerous works have detected and studied thousands of high-z galaxies up to $z \sim 6$ (e.g., Caputi et al. 2015, 2017; Davidzon et al. 2017) and even hundreds of galaxies at higher redshifts (e.g., Stefanon et al. 2021).

At wavelengths $\lambda > 5\,\mu$m, the decreasing instrumental performance coupled with the increasing background noise and the limited lifetime of the cryogenic systems implies that reaching high sensitivities is much more difficult. Indeed, IRAC could reach at most 21–22 mag (5σ) in its extragalactic surveys at 5.8 and 8.0 μm (Euclid Collaboration et al. 2022a). This resulted in a very limited utility of these photometric bands for the study of galaxies at $z > 2$, except for rare, mid-IR bright active galactic nuclei (AGNs; e.g., Stern et al. 2005; Eisenhardt et al. 2012). Similarly, at even longer wavelengths,

observations with The Multiband Imaging Photometer for Spitzer (Rieke et al. 2004) were able to find sources up to $z \sim 3$ (e.g., Le Floc'h et al. 2009; Huynh et al. 2010), but such high redshifts were very rare and above $z \sim 3$ all the detected sources virtually hosted AGNs.

The advent of JWST with its Mid-Infrared Instrument (MIRI; Rieke et al. 2015; Wright et al. 2015) is expected to radically change the ability of mid-IR astronomy to study the high-z universe. The goal of this work is to showcase the major leap forward produced by MIRI from its first observations of extragalactic fields.

In this Letter, we adopt a flat ΛCDM cosmology with $\Omega_\Lambda = 0.7$, $\Omega_m = 0.3$, and $H_0 = 70$ km/s/Mpc. All magnitudes are in the AB photometric system (Oke 1974).

2. Target and Data

Our target is SMACS J0723.3-7327 (hereafter SMACS 0723), a galaxy lensing cluster located in the southern celestial hemisphere (R. A. (J2000.0) = 07^{h}23^{m}19$\overset{s}{.}$5, decl(J2000.0) = $-73°27'15''\!.6$) at $z = 0.39$ (Martinez Aviles et al. 2018). Here we describe the data sets used in our study, which comprise observations from JWST (MIRI, NIRCam) and the Hubble Space Telescope (HST). We also briefly describe the lensing model we adopted to retrieve the physical parameters of our background sources.

2.1. JWST Imaging

The JWST observations of SMACS 0723 (ID proposal: 2736[4], PI: K.M. Pontoppidan) were publicly released as part of the JWST Early Release Observations program on the 2022

[4] https://www.stsci.edu/jwst/phase2-public/2736.pdf

July 13. The observations were carried out with the JWST Near Infrared Camera (NIRCam; Rieke et al. 2005), MIRI (Rieke et al. 2015; Wright et al. 2015), the Near Infrared Imager and Slitless Spectrograph (Willott et al. 2022), and the Near Infrared Spectrograph (NIRSpec; Jakobsen et al. 2022). In the following, we briefly describe the MIRI and NIRCam observations we exploited in our work.

2.1.1. MIRI

The MIRI instrument on board of JWST observed the central region of SMACS 0723 with the wide-band filters F770W, F1000W, F1500W, and F1800W. The observations were carried out on the 2022 June 14, and covered an area of $112\farcs6 \times 73\farcs5$, i.e., the MIRI field-of-view. In this work, we only make use of the F770W image.

We downloaded the fully reduced MIRI images available at the Mikulski Archive for Space Telescopes (MAST).[5] From a visual inspection we found strong background patterns such as vertical stripes and gradients. The intensity of these features varies significantly among filters, thus suggesting that the calibration files available for the MIRI data reduction are not performing well. To improve the background cleaning and homogenization, we decided to rerun the JWST pipeline (version 1.6.1[6]) implementing an ad hoc algorithm able to remove systematics from the fully calibrated exposures generated by the pipeline at the end of stage two and before the final mosaicing performed in stage three. The introduction of this extra step during the data reduction does not only impact on the images cosmetic. In fact, by running and comparing SExtractor catalogs obtained with the same configuration file and based on both the final image obtained with and without the extra step, we found a substantial reduction of spurious detections (especially along the vertical stripes). Contextually, the extra step helped in maximizing the number of real sources detected. Ultimately, to ensure that the extra cleaning of the background did not impact on our magnitude estimates, we compared the magnitudes of bright ($<24\,\mathrm{mag}$) sources. We found no systematic offset between the two estimates.

A comparison between the MIRI and HST images highlighted an astrometric offset between the two data sets. We decided to register the MIRI observations to the HST astronomical coordinate system. To do so, we generated catalogs of sources for all MIRI images and a stacked image of the HST observations via the source extractor software (SExtractor, Bertin & Arnouts 1996). We then matched the catalogs, minimizing the offsets between the detected sources. We found a median offset of ΔR. A. $= 0\farcs50 \pm 0\farcs27$ and Δdecl $= 1\farcs28 \pm 0\farcs08$.

Finally, we resampled the MIRI images to HST via the Python library reproject[7], an affiliated package of Astropy (Astropy Collaboration et al. 2013, 2018).

2.1.2. NIRCam

The NIRCam instrument on board of JWST observed SMACS 0723 with the wide-band filters F090W, F150W, F200W, F277W, F356W, and F444W. The observations were carried out on the 2022 June 6. NIRCam is constituted by two modules (A and B) pointing to adjacent fields of view and covering an area of $2\farcm2 \times 2\farcm2$ (each). For the observations of

---

Table 1
HST and JWST Data for SMACS 0723 Analyzed in This Work

Instrument	Filter	ZPT_{AB} (mag)	f_{ext}	f_{aper}	f_{ZPT}	t_{exp} (ks)
HST/ACS	F435W	25.664	2.047	1.103	⋯	2.2
HST/ACS	F606W	26.500	1.649	1.092	⋯	2.3
HST/ACS	F814W	25.945	1.377	1.094	⋯	2.5
JWST/NIRCam	F090W	26.705	1.291	1.082	1.051	30.1
HST/WFC3 IR	F105W	26.269	1.223	1.136	⋯	1.5
HST/WFC3 IR	F125W	26.230	1.165	1.157	⋯	0.8
HST/WFC3 IR	F140W	26.452	1.138	1.166	⋯	0.8
JWST/NIRCam	F150W	27.052	1.120	1.096	0.979	30.1
HST/WFC3 IR	F160W	25.946	1.115	1.176	⋯	2.1
JWST/NIRCam	F200W	27.233	1.075	1.112	0.970	30.1
JWST/NIRCam	F277W	28.686	1.044	1.122	0.800	7.5
JWST/NIRCam	F356W	28.885	1.029	1.134	0.865	7.5
JWST/NIRCam	F444W	29.002	1.020	1.164	0.956	7.5
JWST/MIRI	F770W	26.556	1.008	1.245	⋯	5.6

Note. For every HST (ACS, WFC3) and JWST (NIRCam, MIRI) filter at our disposal (columns 1 and 2), in this table we report its photometric zero-point ZPT_{AB} (column 3; The JWST photometric zero-points reported in this table have been obtained from $-2.5\log_{10}(\mathrm{PIXAR\_SR} \cdot \mathrm{PHOTMJSR}) - 6.1$, and refer to the flux calibration used in the data reduction (jwst_0916.pmap); to correct for the most updated version of the NIRCam flux calibration (jwst_0989.pmap), the term $-2.5\log_{10}(f_{ZPT})$ should be added to these values), the Galactic extinction correction factor f_{ext} (column 4), the aperture correction factor f_{aper} for a circular aperture of $1''$ diameter (column 5), the correction f_{ZPT} to account for the variation in the JWST/NIRCam photometric zero-points (jwst_0989.pmap) with respect to the flux calibration used in the data reduction (jwst_0916.pmap), and finally, the total exposure time t_{exp} in ks (column 6).

SMACS 0723, only module B targeted the center of the cluster, while module A provided observations for a parallel field.

We downloaded the fully reduced NIRCam images available at MAST. Differently from MIRI, a visual inspection of the data set revealed a good quality of the automatic reduction of NIRCam images by the JWST pipeline. Nonetheless, following the release of the new photometric zero-points of NIRCam (CRDS context jwst_0989.pmap, on 2022 October 3), we corrected the data set at our disposal accordingly; see Table 1.

Also for the NIRCam observations, we used SExtractor to correct the astrometry of the images and register them to the HST data set. In this case, we found a median offset of ΔR. A. $= 1\farcs03 \pm 0\farcs05$ and Δdecl $= 0\farcs01 \pm 0\farcs02$. We finally resampled the NIRCam images to the HST spatial sampling.

2.2. HST Imaging

SMACS 0723 was observed with HST as part of The Reionization Lensing Cluster Survey (RELICS; Coe et al. 2019) that targeted 41 massive galaxy clusters at redshift $z \sim 0.2$–1.0, including 21 of the 34 most massive known according to Planck (Planck Collaboration et al. 2011). The observations of SMACS 0723 were carried out with the F435W, F606W, and F814W filters from the Advanced Camera for Surveys (ACS), and with the F105W, F125W, F140W, and F160W filters from the Wide Field Camera 3 (WFC3) IR channel.

We downloaded the fully reduced HST images from the RELICS repository.[8] Although we used as a reference the RELICS astrometry in our study, we found an offset of

---

ΔR.A. $= -0\rlap{.}{''}53 \pm 0\rlap{.}{''}03$ and Δdecl $= 0\rlap{.}{''}32 \pm 0\rlap{.}{''}01$ when comparing it with the Gaia DR3 catalog (Gaia Collaboration et al. 2022).

2.3. Lensing Model

To derive the demagnified stellar mass of our targets (see Section 4.3), we adopted the recent lensing model of SMACS 0723 by Caminha et al. (2022). The lensing model was obtained using the software `lenstool` (Kneib et al. 1996; Jullo et al. 2007; Jullo & Kneib 2009) to model the mass distribution of the galaxy cluster. In particular, the fiducial mass model was constructed by means of an elliptical cluster-scale dark matter halo, a truncated spherical isothermal mass profile for each cluster galaxy member, and an external shear. The positions of multiple images detected in the JWST/NIRCam images and (when available) spectroscopic redshifts from the Multi-Unit Spectroscopic Explorer (MUSE; Bacon et al. 2010) were adopted to constrain the model. We refer the reader to Caminha et al. (2022) for a more detailed description of the SMACS 0723 lensing model.

3. Photometric Catalog and Sample Selection

After registering and resampling all the images to the same system of coordinates, we constructed our sample. To do so, we extracted photometric catalogs by making use of the software `SExtractor` (Bertin & Arnouts 1996). We ran `SExtractor` in dual mode, using for detection the MIRI 7.7 μm image and measuring the photometry in each of the 14 filters considered here (Table 1). To identify the 7.7 μm sources, we adopted a *hot-mode* configuration (Galametz et al. 2013) and used the weights extension of the MIRI images to improve the rejection of spurious sources.

We measured each source photometry adopting circular apertures of 1′ diameter via the `MAG_APER` task. We corrected these flux estimates for aperture effects f_{aper}; see Table 1. For NIRCam and MIRI, we estimated the aperture correction factor from the `Python` software `WebbPSF` (Perrin et al. 2014).

Whenever dealing with bright and extended sources, circular aperture photometry fails in estimating the galaxy total magnitude. Similarly, it is not suitable for retrieving the photometry of sources significantly stretched by the cluster lensing effect. For these reasons, for all the detected sources in our catalog, we also measured Kron aperture photometry (Kron 1980) via the `SExtractor` task `MAG_AUTO`. In our final catalog we adopt the aperture-corrected `MAG_APER` in all cases with >23 mag, while at <23 mag we kept the brightest measurement between the aperture-corrected `MAG_APER` and `MAG_AUTO`.

Finally, we corrected our photometry for Galactic extinction. This was done by means of the `Python` packages `extinction` and `dustmaps` (Green 2018), and assuming the Galactic extinction curve by Cardelli et al. (1989) with $R_V = 3.1$. We derived values for the color excess E(B-V) in agreement with[9] those by Schlafly & Finkbeiner (2011).

Since `SExtractor` has been found to generally underestimate photometric errors (e.g., Sonnett et al. 2013), we manually set a minimum error of 0.05 mag in all the available filters. This is the value commonly considered as the minimum systematic error for HST imaging data and we adopted it for the JWST observations too.
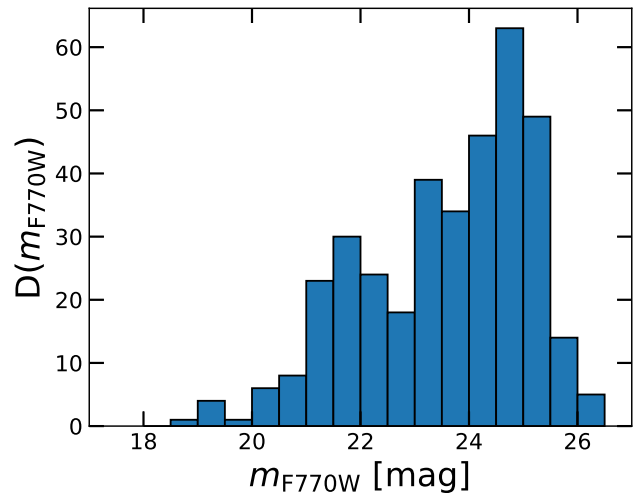
Figure 1. Distribution of JWST F770W magnitudes for our sample of 7.7 μm selected galaxies with S/N(F770W) > 3 and S/N(F356W) > 3 in SMACS 0723. There are 361 sources in total.

Finally, we computed flux upper limits in all cases of a `SExtractor` nondetection. To do so, we masked all sources based on the `SExtractor` segmentation map and estimated the local background flux by randomly placing 1′ diameter apertures in the background and at a maximum distance of 10′ of the nondetected source. After applying a 3σ clipping (until convergence) on the distribution of fluxes retrieved, we obtained the standard deviation (1σ) of the local background. In our final catalog, we consider the 3σ background level as the upper limit on the source flux.
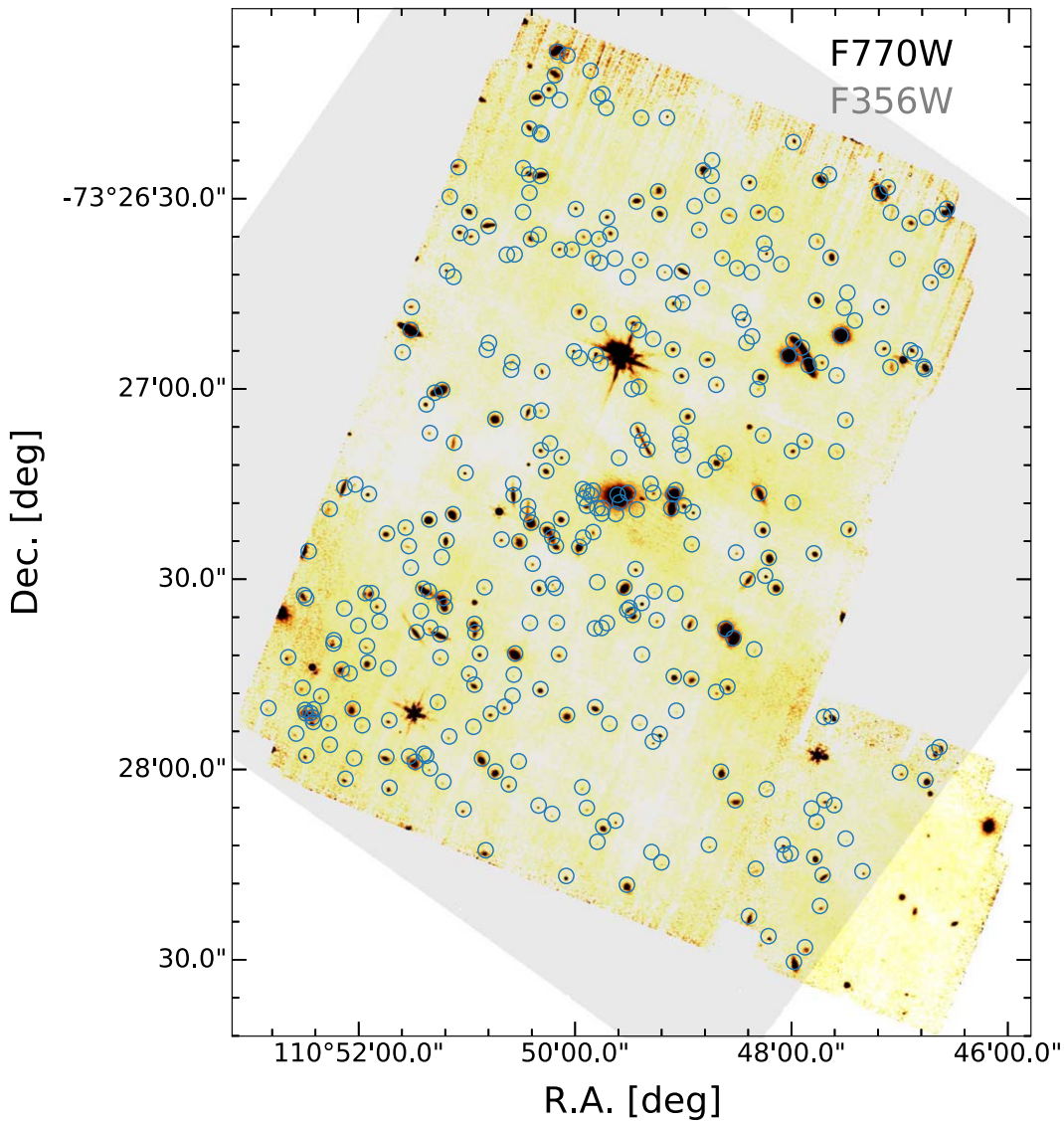
To assess the quality of our photometry, we compared it with the RELICS catalog.[10] The agreement with the RELICS magnitudes allowed us to validate our own photometric measurements. We find a difference between our photometry and the RELICS catalog $\leqslant 0.1$ mag (median) for all the HST filters but for ACS/F435W ($\simeq 0.6$ mag). This wider offset reflects the shallower depth of the filter ($\simeq 23.6$ mag at 5σ) and the fact that our selected sample has F435W magnitudes only between 22 and 24. In addition, we compared our photometry with that provided in the SMACS 0723 photometric catalog obtained by Kokorev et al. (2022). As this catalog includes IRAC photometry at 3.6 and 4.5 μm, we could directly asses the quality of the NIRCam absolute flux calibration at its longest wavelengths. The absence of Spitzer/IRAC observations in channel 4 (8.0 μm) prevented us from verifying the quality of the absolute flux calibration for the MIRI F770W filter.

To construct a reliable sample of sources, we limit our analysis to objects having at least a 3σ detection both at 7.7 μm (MIRI F770W filter) and 3.6 μm (NIRCam F356W filter). We have excluded 11 Galactic stars identified from the Gaia DR3 catalog (Gaia Collaboration et al. 2022) and four other close sources whose reliability and/or photometry are compromised by the bright stellar light.

As a result, we end up with a final sample constituted by 361 sources. We present the F770W magnitude distribution of our sample in Figure 1 and show their spatial distribution in the SMACS 0723 F770W image in Figure 2. The F770W magnitude distribution shows that the number counts increase up to $\sim$25 mag and then we quickly lose completeness at higher

---

[9] https://irsa.ipac.caltech.edu/applications/DUST/

[10] https://archive.stsci.edu/missions/hlsp/relics/SMACS0723-73/catalogs/

Figure 2. Layout of the JWST/MIRI 7.7 μm (F770W) image for SMACS 0723. The open blue circles indicate the spatial position of our final sample of 341 sources having a 3σ detection in both F770W and the JWST/NIRCam F356W filter. The gray-shaded area shows the region of SMACS 0723 covered by the JWST/NIRCam B module.

magnitudes. This is about 2.5 magnitudes deeper than any IRAC 8 μm image available for extragalactic fields.

Figure 3 shows the F356W–F770W color (hereafter [3.6]–[7.7]) of our sources as a function of their F770W magnitude. It is clear that most of the F770W sources are blue, with [3.6]–[7.7] ~ -1. A minority of sources ($\sim$9%) are red instead ([3.6]–[7.7] > 0) and these red sources appear mostly at [7.7] > 24 mag.

4. Spectral Energy Distribution Fitting and Galaxy Derived Parameters

We performed the spectral energy distribution (SED) fitting of our sources by means of the software `LePhare`[11] (Arnouts et al. 1999; Ilbert et al. 2006). For the SED fitting we considered only the photometry up to the NIRCam F444W filter, for a total of 13 HST and NIRCam broad bands (see Figure 1).

We explicitly excluded the MIRI 7.7 μm filter for the modeling because, a priori, we do not know the redshifts of our sources and, thus, we do not know whether the MIRI bands mainly trace stellar or dust emission.

We ran `LePhare` making use of the stellar population synthesis models from Bruzual & Charlot (2003) (hereafter BC03) based on the Chabrier initial mass function (Chabrier 2003), and considering two sets of stellar metallicities: solar ($Z_\odot = 0.02$) and subsolar ($Z = 0.2Z_\odot$). We considered a range of star formation histories (SFHs): an instantaneous burst, i.e., a single stellar population model, and a number of exponentially declining SFHs (τ model), i.e., SFR(t) $\propto e^{-t/\tau}$. For the τ models, we adopted values of τ (the so-called e-folding time) equal to 0.01, 0.1, 0.3, 1, 3, 5, 10, 15 Gyr. We also complemented the BC03 stellar templates with the empirical QSO templates available in `LePhare` from Polletta et al. (2006). To take into account the effects of internal dust extinction, we convolved each synthetic spectrum with the attenuation law by Calzetti et al. (2000) and with the extrapolation proposed by
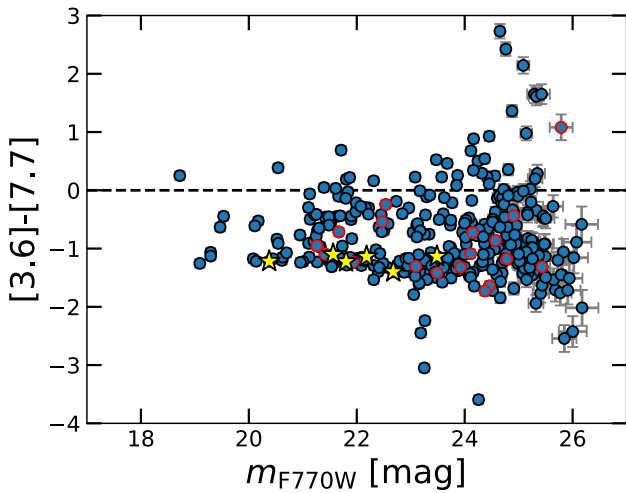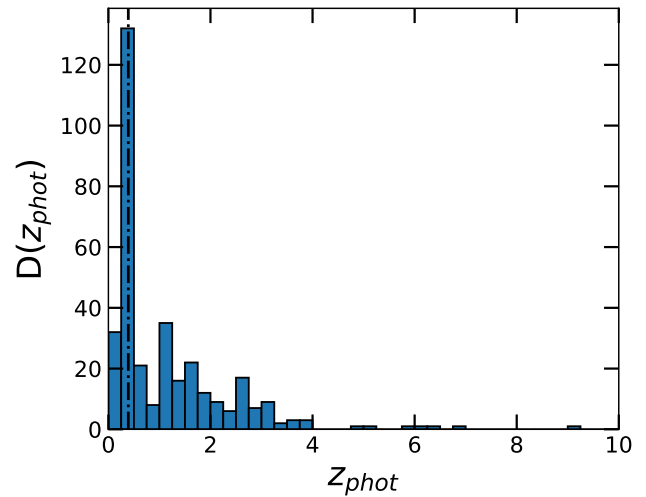
Figure 3. Color magnitude diagram of our sample of 361 7.7 μm selected sources in SMACS 0723. The yellow stars are indicative of the six objects best fitted by stellar templates. Finally, blue circles with red borders show the position of the objects discarded because of their high $\chi^2_{\rm red}$.

Figure 4. Photometric redshift distribution for our 7.7 μm selected source sample in SMACS 0723. The vertical dashed–dotted line indicates the redshift of the SMACS 0723 galaxy cluster ($z = 0.39$).

Leitherer et al. (2002) at short wavelengths, leaving the color excess E(B-V) as a free parameter with values ranging between $0.0 - 1.5$ in steps of 0.1. We ran `LePhare` in the redshift range $z = 0 - 18$ in a mode that takes into account the possible presence of nebular emission lines.

4.1. Photometric Redshifts

From `LePhare`'s output[12] we obtained photometric redshift estimates, as well as derived physical parameters, for all our galaxies. `LePhare` yielded a good SED fit for 96% of all sources (median reduced chi-square $\chi^2_{\rm red} \simeq 1.09$). While, for the remaining 4% (i.e., 14 objects), the code retrieved $\chi^2_{\rm red} > 20$ for all template solutions. We removed these 14 objects from all of our subsequent analysis. By comparing the $\chi^2_{\rm red}$ of the different models, we find six objects with a clear preference for stellar templates ($\Delta\chi^2_{\rm red} > 4$). By looking at their F606W–F814W versus F814W–F356W colors (e.g., Caputi et al. 2011; Weaver et al. 2021), these objects appear to fall along the stellar sequence. For this reason, we discarded these sources from our subsequent analysis. The resulting redshift distribution of the remaining 341 sources is shown in Figure 4.

We compared our photometric redshift estimates with the secure spectroscopic redshifts[13] obtained by Caminha et al. (2022), which were derived from observations with MUSE at the Very Large Telescope. Although the galaxies in our 7.7 μm sample that are detected in MUSE are only 45, we compared the photometric redshifts and spectroscopic values for the common sources. Out of this matched sample, we identified five sources (11%) as *catastrophic outliers*, i.e., $|z_{\rm phot} - z_{\rm spec}|/(1 + z_{\rm spec}) > 0.15$. We derived a negligible bias for the $|z_{\rm phot} - z_{\rm spec}|/(1 + z_{\rm spec}) \leqslant 0.15$ population (median($z_{\rm phot} - z_{\rm spec}) = 0$), and a tight $z_{\rm phot} - z_{\rm spec}$ correlation (standard deviation $\sigma = 0.04$). Overall, this confirmed the reliability of our photometric estimates.

As an additional check, we investigated the impact of possible secondary $z_{\rm phot}$ solutions to our findings. According to `LePhare`, 14% of our sample (49 objects) has a secondary redshift solution $z_{\rm SEC}$ such as $|z_{\rm BEST} - z_{\rm SEC}| > 0.5$ and $|\chi^2_{\rm red,BEST} - \chi^2_{\rm red,SEC}| < 4$. Nonetheless, if we chose to adopt the secondary $z_{\rm phot}$ solution for these sources, we would not observe any substantial change in the overall redshift distribution of our sample nor for the trends on the derived physical quantities discussed in the following. This result suggests that our findings are robust against degeneracies in redshift space.

Figure 4 shows that the 7.7 μm galaxy population spans a very wide redshift range from $z = 0$ through $z \sim 9.2$, with 57% of the sources lying at $z < 1$ and the remaining 43% at higher redshifts. Sources above $z = 4$ constitute 2% of our sample. The observed 7.7 μm flux corresponds to rest-frame wavelengths, which at different redshifts, trace very different physical processes. At $z < 1$, the observed 7.7 μm emission is dominated by the galaxy hot dust emission. At higher redshifts, the 7.7 μm wavelength domain becomes increasingly dominated by stellar emission. Therefore, the breadth of the redshift distribution indicates the varied nature of the 7.7 μm selected sources.

For the sources with an estimate of $z_{\rm phot} > 1$ (145 objects in total), we decided to rerun `LePhare` adding the MIRI photometric measurement at 8 μm. From this additional test, we confirmed the photometric redshift for 87% of these sources (126 objects), while for the remaining 13% (19 objects) we obtained a difference with the previous $z_{\rm phot}$ estimate larger than 0.5. However, by comparing the $\chi^2_{\rm red}$ of the two solutions, no objects were found to have a significantly better reduced chi-square, i.e., $\Delta\chi^2_{\rm red} > 4$. Hence, we kept the best results obtained by fitting only the HST and JWST/NIRCam photometry.

4.2. NIRCam/MIRI Colors and Galaxy Internal Extinctions

The varied nature of the 7.7 μm source population is also illustrated in Figure 5. Even at similar redshifts, galaxies span a range of [3.6]–[7.7] colors.

---

[12] The complete photometric information as well as the physical properties of our final sample of 341 sources is presented in an electronic table available at https://gitlab.astro.rug.nl/iani/smacs0723/. In Table 2 we present an excerpt of it, reporting the properties derived for the four sources at $z_{\rm phot} > 6$ we found in our sample (see Section 4.4).

[13] https://wwwmpa.mpa-garching.mpg.de/~caminha/SMACS0723_Caminha/model_JWST_v01/
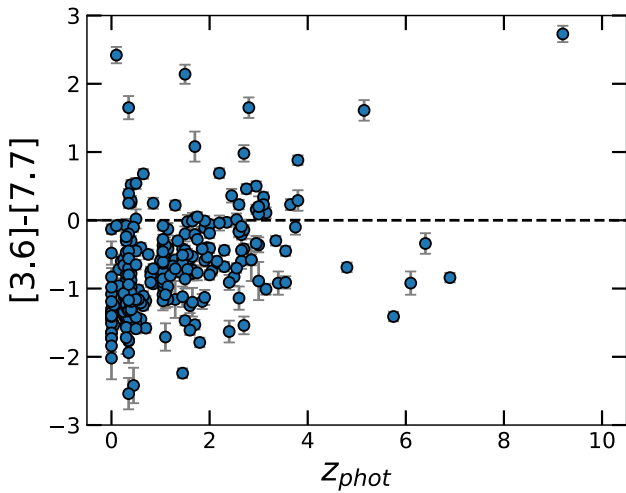
Figure 5. [3.6]–[7.7] vs. photometric redshift z_{phot} for our 7.7 μm selected galaxy sample.

The best-fit SEDs of the 7.7 μm sources are characterized by a wide range of A_V values (Figure 6). Only a minority ($<10\%$) require high dust extinctions ($A_V > 2$ mag) for the SED fitting and are virtually all sources at $z < 3$ in our sample. Interestingly, the sources with red color $[3.6] - [7.7] > 0$ do not preferentially correspond to cases with high A_V values.

Stern et al. (2005) proposed to isolate potential AGNs using IRAC [3.6]–[4.5] versus [5.8]–[8.0] colors. Unfortunately we do not have MIRI 5.6 μm photometry for SMACS 0723, but we can analyze [3.6]–[4.4] colors instead. We find that we only have a few sources with $[3.6]-[4.4] > 0$ at $z > 2$, so AGNs with an IR power law do not seem to be a significant fraction of our high-z sample (the surface density of these sources is likely too low to see them in significant numbers in the small area covered by SMACS 0723).

4.3. Stellar Masses of z > 1 Galaxies

For completeness, we also analyze the derived stellar masses for our galaxies. As SMACS 0723 is a lensing cluster, the stellar masses of background sources need to be corrected by lensing magnification. We used the lensing model by Caminha et al. (2022) (see Section 2.3) to correct these stellar masses for magnification. The lensing-corrected stellar mass versus z_{phot} for all our galaxies at $z > 1$ is shown in Figure 7. The median magnification factor for our sample is $\mu = 2.56$. About 11% of sources above $z > 1$ (i.e., 5% of the overall sample) have a magnification factor above 10 and they are all objects with $z_{phot} < 4$ (see Figure 7).

The 7.7 μm source sample contains galaxies with a wide range of stellar masses 10^7–$10^{11} M_\odot$ at $z > 1$, indicating that a selection in this wave band does not necessarily correspond to a selection in stellar mass even at $z > 1$. Nevertheless, it should be noted that the sparse population of the stellar-mass plot at $z > 4$ is to some extent due the fact that these galaxies are increasingly rarer toward higher redshifts and the area sampled by SMACS 0723 is small. So not all stellar-mass galaxies at high z might be represented in this field due to sample variance, but this is not because of a consequence of the 7.7 μm selection.

This is also true for the highest redshift sources at $z > 6$ in our sample. A few of them have stellar masses $10^8 - 10^9 M_\odot$, while one has $\sim 2 \times 10^{10} M_\odot$, i.e., it is quite massive for such
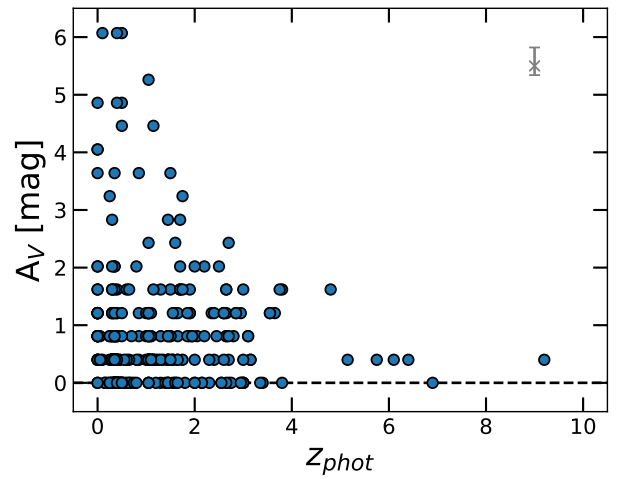
Figure 6. Dust extinction A_V as a function of photometric redshift z_{phot}. In the top right corner we report in gray the typical (median) value of the error associated to the A_V estimate.
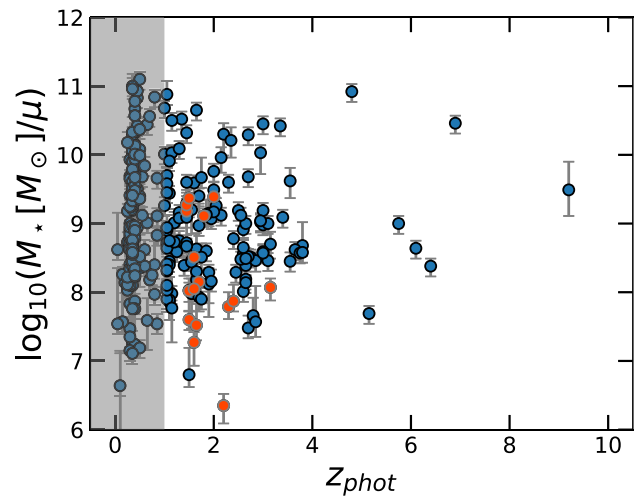

Figure 7. Diagram of the stellar mass (corrected for lensing magnification) of our sample of sources as a function of the photometric redshift z_{phot}. The orange circles identify the objects with a magnification factor μ above 10, while the shaded area highlights the region of the diagram where $z_{phot} < 1$.

high redshifts (see Section 4.4). In fact, even though galaxies with stellar masses $M_\star \sim 10^{10} M_\odot$ at $z \sim 7$ have been previously found with Spitzer, they were only detected in IRAC channels 1 and 2 (e.g., Roberts-Borsani et al. 2016; Euclid Collaboration et al. 2022b), and not at longer wavelengths.

4.4. 7.7 μm Sources at z > 6

Figures 8 and 9 show postage stamps and the best-fit SEDs of all our galaxies at $z_{phot} > 6$. The postage stamps show their clear detection at both 7.7 and 3.6 μm. In both cases, the resulting SED fitting is of very good quality. For ID 382, even the 7.7 μm photometric point, which was not used for the SED fitting, is in excellent agreement with the extrapolation of the best-fit template at observed wavelengths $>5 \mu$m.

Source ID 138 at $z_{phot} = 6.4$ has a best-fit dust extinction $A_V = 0.4$ mag and a delensed stellar mass of $2.4 \times 10^8 M_\odot$ (magnification factor $\mu = 4.02 \pm 0.46$). Similarly, ID 382 at $z_{phot} = 6.1$ ($\mu = 2.86 \pm 0.13$) has $A_V = 0.4$ mag and a delensed stellar mass of $4.3 \times 10^8 M_\odot$. ID 399 at $z_{phot} = 6.9$ ($\mu = 2.32 \pm 0.05$), instead, has a visual extinction $A_V = 0$ mag and a
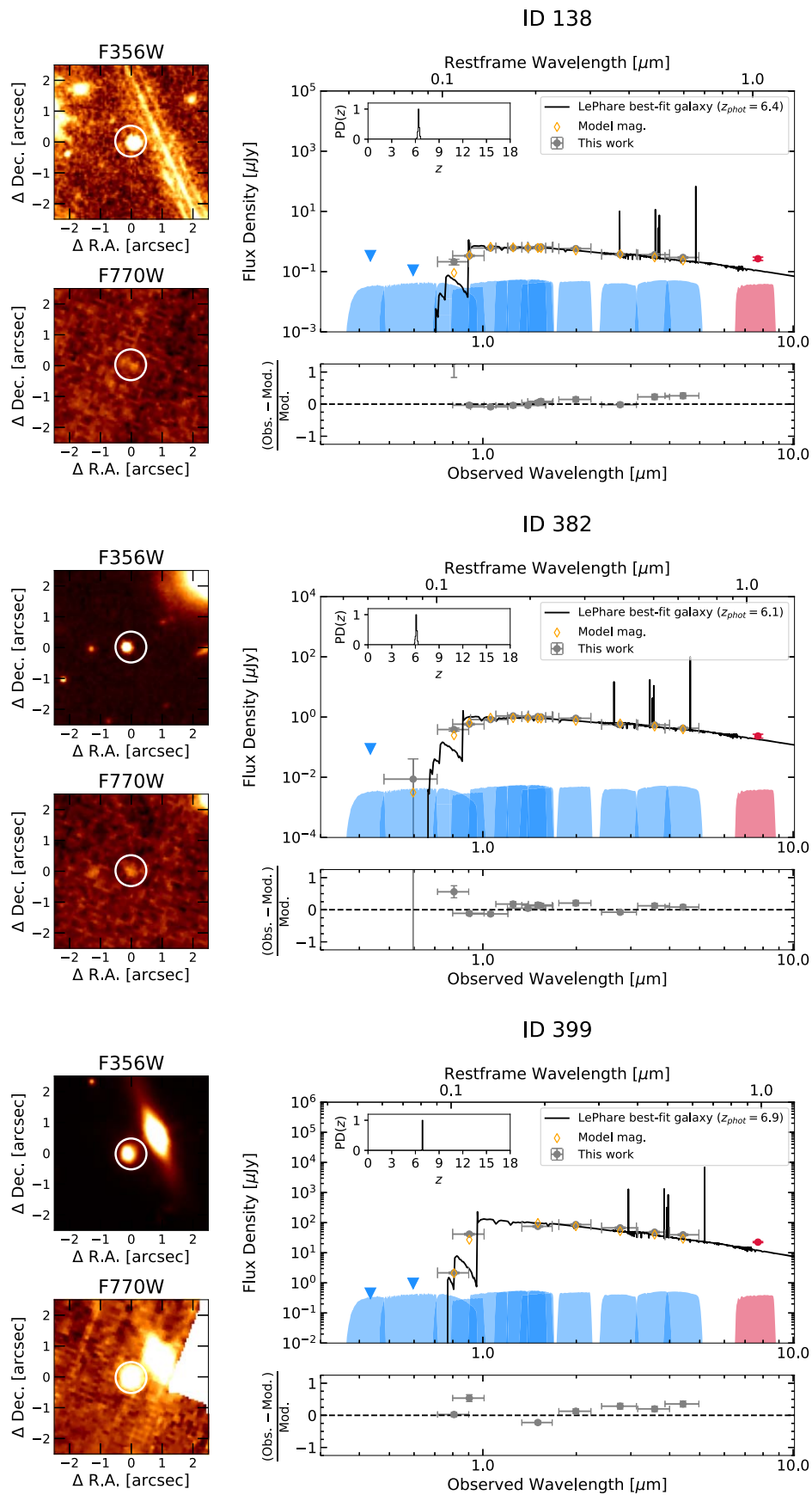
Figure 8. LePhare best-fit SED of galaxies ID 138 (top), ID 382 (center), and ID 399 (bottom), both at $z_{phot} > 6$. The MIRI 7.7 μm point (in red) has not been used for the SED fitting, but added a posteriori. The inset in the top-left corner shows the probability distribution for the estimate of the photometric redshifts z_{phot} (PDZ). For the three galaxies, we show cutout images ($5'' \times 5''$) in the NIRCam F356W and MIRI F770W bands.
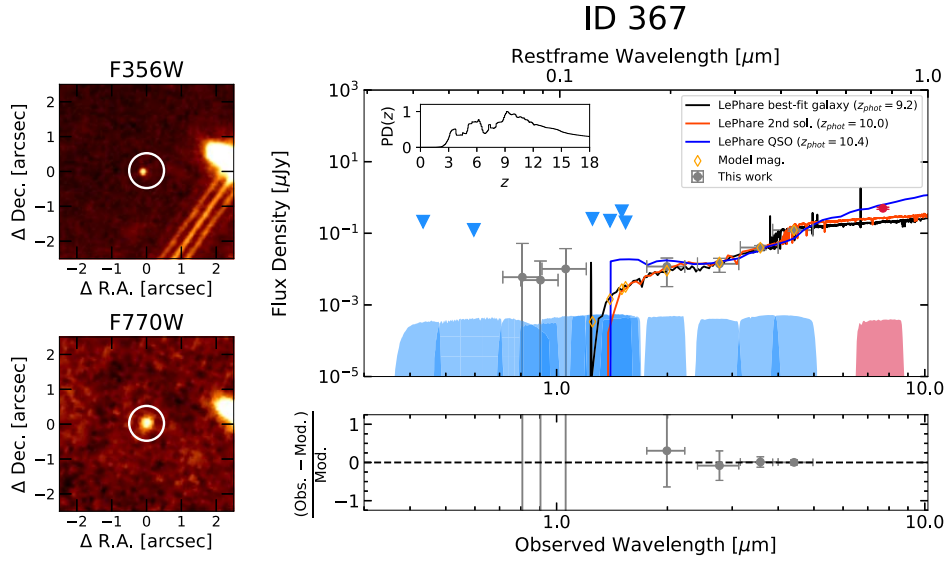
ID 367

Figure 9. `LePhare` best-fit SED of galaxy ID 367 at $z_{phot} = 9.2$ (in black). The orange and blue spectra show `LePhare` best-fit secondary galaxy solution ($z_{phot} = 10$) and quasi-stellar object (QSO) template ($z_{phot} = 10.4$), respectively. The MIRI 7.7 μm point has not been used for the SED fitting, but added a posteriori. The inset in the top-left corner shows the PDZ of this source. On the left-hand side panels, we show cutout images ($5'' \times 5''$) of ID 367 in the NIRCam F356W and MIRI F770W bands.

delensed stellar mass $\sim 2 \times 10^{10} M_\odot$. Interestingly, all these sources are not affected by strong magnification ($\mu \sim 2 - 4$), thus suggesting that future deeper MIRI observations at 7.7 μm will be able to detect such objects even in nonlensed fields. In Table 2, we report all the photometric information we derived for these sources as well as their inferred physical properties.

The last object with $z_{phot} > 6$ is ID 367. This is the source with the highest photometric redshift estimate out of all of our sample, i.e., $z_{phot} = 9.2$. As shown in Figure 9, this source has a complex redshift probability distribution (PDZ), with a secondary photometric solution at $z_{phot} = 10$ and a solution from the QSO models with $z_{phot} = 10.4$. Despite the fact that best-fit models prefer high-z solutions, low-z solutions cannot be completely ruled out as pointed out by the breadth of the PDZ, which extends down to $z \sim 3$. The SED of this object shows a clear and steep rise above 2 μm and, interestingly, the QSO template seems to nicely predict the observed 8 μm flux of this source. Nonetheless, based on the χ^2_{red}, `LePhare` does not present a clear preference among the different best-fit models ($|\Delta \chi^2_{red}| \lesssim 0.2$ in all cases). Besides, by rerunning the SED fitting considering the MIRI F770W filter, the photometric redshift solutions do not appear to vary significantly ($\Delta z_{phot} \leqslant 0.5$) and, at the same time, the χ^2_{red} does not improve ($|\Delta \chi^2_{red}| \lesssim 0.3$). For this object, we estimate an $A_V = 0.4$ mag and a stellar mass of $3 \times 10^9 M_\odot$. ID 367 was also reported by Rodighiero et al. (2022) (dubbed in their catalog as `PENNAR`) with a primary photometric solution $z_{phot} = 12.1$, a visual extinction $A_V \simeq 2.5$ mag, and a stellar mass $\sim 4 \times 10^9 M_\odot$. We ascribe the differences in the results as due to the diverse technique of SED fitting performed, the differences in the photometric NIRCam zero-points applied, as well as to the fact that we do not implement the MIRI longer-wavelength filters (>8 μm) in our SED fit.

5. Summary and Conclusions

In this Letter we have presented the first physical-parameter characterization of the 7.7 μm selected galaxy population based on JWST MIRI and NIRCam data. We studied the lensing

cluster SMACS 0723, which was one of the first extragalactic fields observed with JWST. We complemented the JWST data with ancillary HST images, allowing us to perform the galaxy SED fitting on a total of 13 broad bands for our total population of 341 7.7 μm selected galaxies with $S/N > 3$ in both F770W and F356W.

We obtained photometric redshifts and other derived physical parameters for all our sources. We showed that at the depth of the current MIRI survey, the 7.7 μm selection results in a heterogenous galaxy population: 57% of the selected galaxies are at $z < 1$ for which the 7.7 μm light should be mostly produced by hot dust emission. The other 43% correspond to galaxies at $z > 1$, a redshift regime where the 7.7 μm light is increasingly dominated by stellar emission. Our high-z sample has a small tail (2%) of objects at $z > 4$, which reaches $z = 9.2$, indicating that already at these depths the MIRI 7.7 μm images contain galaxies within the epoch of reionization.

All the objects in our final sample are best fit with galaxy templates. In addition, one of our galaxies (ID 146) at $z_{phot} = 2.7$ is an Atacama Large Millimeter/submillimeter Array (ALMA) millimeter source observed in the ALCS program (P.I. K. Kohno; see Sun et al. 2022).

The vast majority of the 7.7 μm galaxies have blue [3.6]–[7.7] colors, independent of redshift. Less than 10% of them have red colors [3.6] − [7.7] > 0 and this red color is not necessarily associated with high A_V values. Although the 7.7 μm galaxies span a wide range of best-fit A_V values, only a few of them at $z < 2$ seem to need the maximum $A_V \approx 6$ mag permitted in our SED-fitting runs.

The $z > 1$ galaxies in our sample span stellar masses between 10^7 and $10^{10} M_\odot$. The access to low stellar masses is facilitated thanks to the gravitational lensing effect, as it has been shown by previous works (e.g., Rinaldi et al. 2022). We do not find any very massive $>10^{11} M_\odot$ galaxies, but this is not surprising, given the small volume sampled by the SMACS 0723 field. Concurrently, we found that the extension of our sample to high-z sources ($z > 6$) is not driven by lensing magnification (average magnification factors $\mu \simeq 2$–4). This suggests that

Table 2
Main Properties of Our Sample of 7.7 μm Detected Sources at $z_{phot} > 6$ (Excerpt of the Electronic Table Reporting the Properties of the 341 Sources of Our Final Sample)

ID	R.A. (deg)	Decl (deg)	f_{F435W} (nJy)	f_{F606W} (nJy)	f_{F814W} (nJy)	f_{F090W} (nJy)	f_{F105W} (nJy)	f_{F125W} (nJy)	f_{F140W} (nJy)
138	110.862082	−73.462243	339.99[a]	112.44[a]	215.02 ± 31.01	340.10 ± 15.66	614.75 ± 28.31	620.47 ± 30.59	613.09 ± 28.23
367	110.819567	−73.444912	211.97[a]	125.44[a]	6.01 ± 31.03	4.98 ± 7.99	10.21 ± 18.33	255.49[a]	226.05[a]
382	110.842626	−73.444114	88.35[a]	8.74 ± 21.55	387.53 ± 31.05	583.23 ± 26.86	832.42 ± 38.33	1095.27 ± 50.44	973.58 ± 44.83
399	110.776827	−73.442334	452.88[a]	959.86[a]	2167.61 ± 99.82	41870.86 ± 1928.23	...	...	...

f_{F150W} (nJy)	f_{F160W} (nJy)	f_{F200W} (nJy)	f_{F277W} (nJy)	f_{F356W} (nJy)	f_{F444W} (nJy)	f_{F770W} (nJy)
648.40 ± 29.86	666.24 ± 30.68	586.16 ± 27.00	377.19 ± 17.37	369.25 ± 17.01	298.45 ± 13.75	269.09 ± 34.33
414.71[a]	203.24[a]	11.91 ± 5.75	14.17 ± 3.98	40.42 ± 3.66	123.55 ± 5.69	499.57 ± 34.36
1041.02 ± 47.94	1013.60 ± 46.68	915.56 ± 42.17	568.88 ± 26.20	548.16 ± 25.24	428.27 ± 19.72	234.05 ± 34.36
75889.15 ± 3494.82	...	86764.42 ± 3995.65	67527.70 ± 3109.77	48620.38 ± 2239.05	39783.05 ± 1832.08	22461.64 ± 1034.40

[3.6]–[7.7]	z_{BEST}	z_{SEC}	A_V (mag)	$\chi^2_{red,\,BEST}$	μ	$\log_{10}(M_{\star,delens})$ ($M_\odot$)
−0.34 ± 0.15	6.40	...	$0.40^{+0.20}_{-0.12}$	1.96	4.02 ± 0.46	$8.38^{+0.11}_{-0.15}$
+2.73 ± 0.12	9.2	10.0	$0.40^{+0.81}_{-0.40}$	1.07	3.60 ± 0.20	$9.49^{+0.41}_{-0.38}$
-0.92 ± 0.17	6.1	...	$0.40^{+0.16}_{-0.12}$	3.66	2.86 ± 0.13	$8.64^{+0.11}_{-0.15}$
-0.84 ± 0.07	6.9	...	0.0	2.13	2.32 ± 0.05	$10.46^{+0.11}_{-0.14}$

Note. All the physical parameters presented and discussed in this Letter for our final sample of 341 7.7μm detected sources in SMACS 0723 are available at https://gitlab.astro.rug.nl/iani/smacs0723/.
[a] In this table, † is indicative of photometric measurements for which we have only an upper limit.

(This table is available in its entirety in machine-readable form.)

deeper MIRI 7.7 μm observations will be able to detect such high-z objects even in nonlensing fields.

Overall, this work demonstrates the enormous potential of MIRI to open up the study of the high-redshift universe at mid-IR wavelengths, particularly at 7.7 μm where MIRI still has relatively high sensitivity. Very soon, deeper MIRI 7.7 μm observations will be available, allowing us to investigate a larger number of high-z galaxies, all the way into the epoch of reionization.

ORCID iDs

Edoardo Iani https://orcid.org/0000-0001-8386-3546
Karina I. Caputi https://orcid.org/0000-0001-8183-1460
Pierluigi Rinaldi https://orcid.org/0000-0002-5104-8245
Vasily I. Kokorev https://orcid.org/0000-0002-5588-9156

References

Arnouts, S., Cristiani, S., Moscardini, L., et al. 1999, MNRAS, 310, 540
Astropy Collaboration, Price-Whelan, A. M., Sipőcz, B. M., et al. 2018, AJ, 156, 123
Astropy Collaboration, Robitaille, T. P., Tollerud, E. J., et al. 2013, A&A, 558, A33
Bacon, R., Accardo, M., Adjali, L., et al. 2010, Proc. SPIE, 7735, 773508
Bertin, E., & Arnouts, S. 1996, A&AS, 117, 393
Bradač, M. 2020, NatAs, 4, 478
Bruzual, G., & Charlot, S. 2003, MNRAS, 344, 1000
Calzetti, D., Armus, L., Bohlin, R. C., et al. 2000, ApJ, 533, 682
Caminha, G. B., Suyu, S. H., Mercurio, A., et al. 2022, A&A, 666, L9
Caputi, K. I., Cirasuolo, M., Dunlop, J. S., et al. 2011, MNRAS, 413, 162
Caputi, K. I., Deshmukh, S., Ashby, M. L. N., et al. 2017, ApJ, 849, 45
Caputi, K. I., Ilbert, O., Laigle, C., et al. 2015, ApJ, 810, 73
Cardelli, J. A., Clayton, G. C., & Mathis, J. S. 1989, ApJ, 345, 245
Chabrier, G. 2003, PASP, 115, 763

Coe, D., Salmon, B., Bradač, M., et al. 2019, ApJ, 884, 85
Davidzon, I., Ilbert, O., Laigle, C., et al. 2017, A&A, 605, A70
Dole, H., Lagache, G., Puget, J. L., et al. 2006, A&A, 451, 417
Eisenhardt, P. R. M., Wu, J., Tsai, C.-W., et al. 2012, ApJ, 755, 173
Euclid Collaboration, Moneti, A., McCracken, H. J., et al. 2022a, A&A, 658, A126
Euclid Collaboration, van Mierlo, S. E., Caputi, K. I., et al. 2022b, A&A, 666, A200
Fazio, G. G., Hora, J. L., Allen, L. E., et al. 2004, ApJS, 154, 10
Gaia Collaboration, Vallenari, A., Brown, A. G. A., et al. 2022, arXiv:2208.00211
Galametz, A., Grazian, A., Fontana, A., et al. 2013, ApJS, 206, 10
Green, G. 2018, JOSS, 3, 695
Huynh, M. T., Gawiser, E., Marchesini, D., Brammer, G., & Guaita, L. 2010, ApJ, 723, 1110
Ilbert, O., Arnouts, S., McCracken, H. J., et al. 2006, A&A, 457, 841
Jakobsen, P., Ferruit, P., Alves de Oliveira, C., et al. 2022, A&A, 661, A80
Jullo, E., & Kneib, J. P. 2009, MNRAS, 395, 1319
Jullo, E., Kneib, J. P., Limousin, M., et al. 2007, NJPh, 9, 447
Kneib, J. P., Ellis, R. S., Smail, I., Couch, W. J., & Sharples, R. M. 1996, ApJ, 471, 643
Kokorev, V., Brammer, G., Fujimoto, S., et al. 2022, arXiv:2207.07125
Kron, R. G. 1980, ApJS, 43, 305
Le Floc'h, E., Aussel, H., Ilbert, O., et al. 2009, ApJ, 703, 222
Leitherer, C., Li, I. H., Calzetti, D., & Heckman, T. M. 2002, ApJS, 140, 303
Martinez Aviles, G., Johnston-Hollitt, M., Ferrari, C., et al. 2018, A&A, 611, A94
Oke, J. B. 1974, ApJS, 27, 21
Perrin, M. D., Sivaramakrishnan, A., Lajoie, C.-P., et al. 2014, Proc. SPIE, 9143, 91433X
Planck Collaboration, Ade, P. A. R., Aghanim, N., et al. 2011, A&A, 536, A1
Polletta, M. d. C., Wilkes, B. J., Siana, B., et al. 2006, ApJ, 642, 673
Rieke, G. H., Wright, G. S., Böker, T., et al. 2015, PASP, 127, 584
Rieke, G. H., Young, E. T., Engelbracht, C. W., et al. 2004, ApJS, 154, 25
Rieke, M. J., Kelly, D., & Horner, S. 2005, Proc. SPIE, 5904, 1
Rinaldi, P., Caputi, K. I., van Mierlo, S. E., et al. 2022, ApJ, 930, 128
Roberts-Borsani, G. W., Bouwens, R. J., Oesch, P. A., et al. 2016, ApJ, 823, 143
Rodighiero, G., Bisigello, L., Iani, E., et al. 2022, MNRAS Letters, 518, L19
Schlafly, E. F., & Finkbeiner, D. P. 2011, ApJ, 737, 103
Sonnett, S., Meech, K., Jedicke, R., et al. 2013, PASP, 125, 456
Stefanon, M., Labbé, I., Oesch, P. A., et al. 2021, ApJS, 257, 68
Stern, D., Eisenhardt, P., Gorjian, V., et al. 2005, ApJ, 631, 163
Sun, F., Egami, E., Fujimoto, S., et al. 2022, ApJ, 932, 77
Weaver, J. R., Kauffmann, O., Shuntov, M., et al. 2021, BAAS, 53, 2021n1i215p06
Werner, M. W., Roellig, T. L., Low, F. J., et al. 2004, ApJS, 154, 1
Willott, C. J., Doyon, R., Albert, L., et al. 2022, PASP, 134, 025002
Wright, G. S., Wright, D., Goodson, G. B., et al. 2015, PASP, 127, 595